Background-suppressed Infrared Photothermal Microscopy at Low Temperature

Thao N. Pham[*] Jiaze Yin[*] Yuhao Yuan, Dingcheng Sun, Bethany Weinberg, Hongli Ni, Ji-Xin Cheng [◊]

KEYWORDS: photothermal, short-wave infrared, mid-infrared, temperature, infrared spectroscopy

ABSTRACT. The shortwave-infrared region provides reduced scattering and improved penetration depth compared to visible and near-infrared wavelengths. However, strong water absorption across this spectral window generates background signals that limit contrast and obscure weak biomolecular features. To address this challenge, we implement a low-temperature approach that exploits the temperature dependence of the water photothermal response to suppress background while preserving lipid-derived signal in photothermal microscopy. Sample cooling during imaging enhanced the signal-to-background ratio (S/B) by up to 5.5-fold in cellular imaging and improved the contrast-to-noise ratio (CNR) of weak lipid features by up to 1.6-fold at greater tissue depths, enabling reliable volumetric imaging in complex biological systems. We further show that low-temperature approach is also applicable to mid-infrared photothermal microscopy, thus providing an effective means to enhance photothermal contrast of aqueous specimens.

1 INTRODUCTION

The shortwave infrared (SWIR) window, typically between 1000 nm to 2000 nm, offers an optical window with significantly reduced photon scattering and minimal tissue autofluorescence compared to the visible and near-infrared regions [1,2]. A variety of imaging strategies have been developed to harness these advantages. SWIR fluorescence imaging leverages penetration depth for tumor detection [3], whereas broader applications are limited by the biocompatible fluorophores that emit efficiently in SWIR region. Importantly, the SWIR region provides access to overtone and combination vibrational modes of molecular bonds, presenting a unique opportunity for label-free deep imaging. SWIR spectroscopy and microscopy have garnered increasing attention for applications in deep-tissue biomedical imaging, including chemical mapping [4], tumor visualization [5–8] and functional imaging [9–11]. However, direct SWIR imaging relies on negative contrast, where increased absorption from molecular bonds leads to decrease signal intensity, as described by the Beer–Lambert law [12,13]. This absorption-based contrast is fundamentally limited by the strong background signal from water, which exhibits broad absorption across the SWIR spectrum and can mask weaker endogenous vibrational signals, reduce chemical specificity, and limit the imaging depth.

To mitigate the direct contribution of water absorption, infrared photothermal microscopy was recently developed as an alternative to conventional absorption-based detection [14]. SWIP is a label-free pump-probe imaging technique that indirectly measures absorption by the photothermal effect. Specifically, a pulsed laser selectively excites certain chemical bonds in the target molecule, generating a heat that increases the local temperature, causing a change of refractive index (RI) of the surrounding environment detected by a probe beam. SWIP enables imaging depths of up to 1 mm while maintaining micrometer-scale resolution[14,15]. This depth-

resolution balance makes SWIP well-suited for resolving submicron structures in complex thick biological samples.

Even with the excitation wavelength tuned to the resonant absorption peaks of target biomolecules, cumulative water absorption increases with depth, overwhelming weak biomolecular signals and ultimately reducing contrast and sensitivity in deeper layers. To solve the residual water background issue in photothermal imaging, time-resolved measurement is proposed. By leveraging the thermal decay differences, biomolecules such as proteins and lipids can be separated from water [14,16,17]. Although contrast is enhanced, this approach still measures the induced water photothermal signal and requires time-intensive post-processing.

We notice that liquid water molecules exhibit a unique property: the density reaches maximum around 4°C [18]. This phenomenon was explored in optoacoustic spectroscopy [19,20], where water becomes optoacoustically mute at 4°C. Since the photothermal contrast originates from changes in RI, which is closely related to density, we report an effective strategy for background suppression in photothermal imaging by lowering temperature of the sample to near 4°C. We hypothesized that reducing the sample temperature would suppress the non-specific water background, thereby improving signal-to-background ratio (S/B) and contrast-to-noise ratio (CNR), even in deep layers of volumetric samples. To test our hypothesis, we built a perfusion system into the microscope to cool down sample dishes and performed low-temperature SWIP imaging. We validated this approach across a range of biological models, including culture cells, live *C. elegans,* and tissues sections. In all cases, our approach selectively minimizes water contributions while preserving the vibrational contrast of target biomolecules in the SWIR region.

After validating the ability to reduce water background using low temperature, we further extended this strategy into mid-infrared region, which vibrational features are more chemically informative but water-induced background is more severe. In that case, we achieved up to 2.8-fold improvement in S/B for cell in PBS when imaging the amide-I band, which spectrally overlaps with water O-H bending mode.

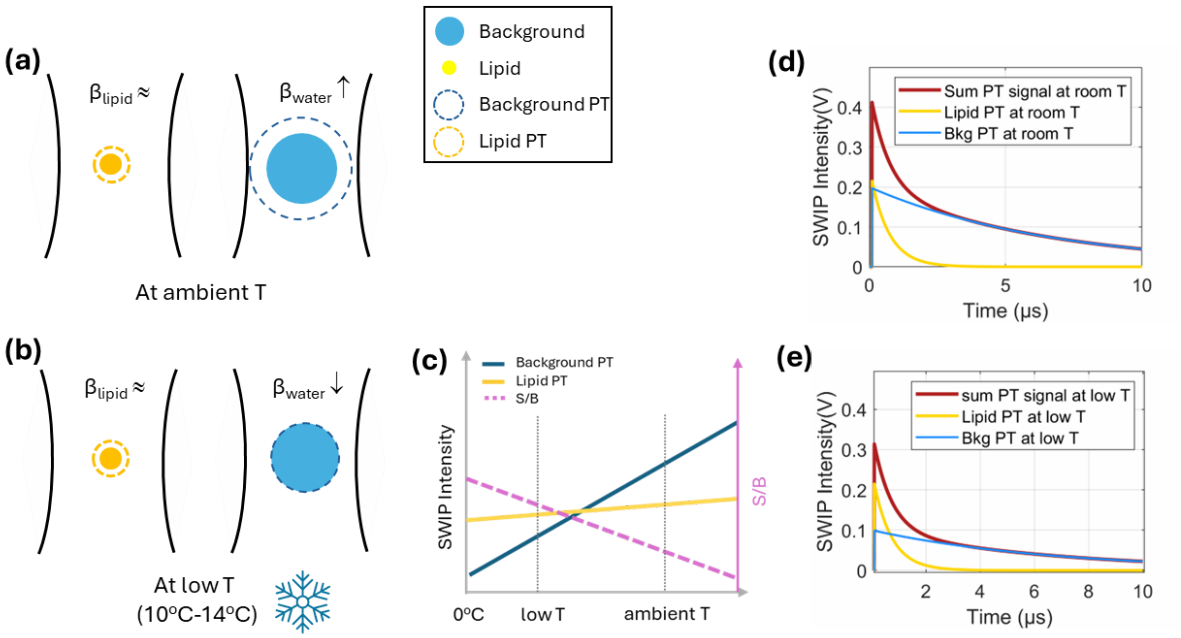


Figure 1: Principle of low temperature photothermal spectroscopy. (a) Particles and water PT response at ambient temperature. (b) Particles and water PT response at low temperature. (c) Conceptual illustration of the temperature dependence of SWIP signal S/B. (d, e), Simulated SWIP traces and their components at ambient and low temperature, respectively, corresponding to the gray dashed line in (c). Red line represents the raw SWIP signal, which can be decomposed into two components based on their distinct thermal decay profiles: a fast decay for lipid signal (yellow) and slow decay for water signal (blue). At low temperatures, water signals are suppressed while lipid signals persist, resulting in a lower total PT intensity but improved S/B. PT: photothermal. ≈: unchanged.

2 TEMPERATURE DEPENDENCY OF OPTICALLY DETECTED PHOTOTHERMAL SIGNAL

Theoretically, the SWIP signal is measured as the modulated probe power , and can be described as [21]

(1)

where is the temperature change due to photon absorption, is the thermo-optic coefficient, and is the power of the probe beam. The thermo-optic coefficient characterizes how sensitively the RI change (responds to the temperature change [22]

(2)

To further understand how RI responds to temperature, we consider the simplified Lorentz–Lorenz equation, which relates the refractive index (to the density [23–25]

(3)

whereis the Lorentz–Lorenz coefficient, which depends on the polarizability of the molecule and remains constant within our studied temperature range [26]. Then, by taking the derivative and simplifying the equation (supplementary S2), we have the relationship

(4)

By relating (4) to (2) and (1), the thermo-optic coefficient and the SWIP intensity are directly governed by how density changes () with temperature.

(5)

In SWIP imaging, we detect PT signal from lipid particles, while water mostly contributes to the background signal. We then have

(6)

(7)

Therefore, the signal-to-background ratio (S/B) in SWIP imaging is defined as the ratio of and

(8)

becomes smaller as the water density reaches inflection point at 4°C [18,27], while is unchanged [28] (**Figure 1a, b**). **Figure 1c** provides a conceptual illustration of this temperature-dependent relationship, showing that cooling reduces the water background photothermal signal while relatively preserving the lipid signal, thereby increasing the signal-to-background ratio (S/B). **Figures 1d** and **1e** show representative stimulated SWIP traces acquired under ambient and low temperature conditions. The raw SWIP signal, shown as a red solid line, can be decomposed into two components based on their distinct thermal decay profiles [14]. The first component, attributed primarily to the water background, exhibits a slower thermal decay, shown as the blue solid line. The second component, representing the lipid signal, displays a faster decay, shown as the yellow solid line. Upon lowering the sample temperature, the photothermal signal from water is significantly suppressed, while the lipid signal remains detectable. These simulations led us to hypothesize that photothermal imaging at low temperatures can enhance the (S/B) by selectively suppressing the water-derived background.

3 LOW-TEMPERATURE SHORTWAVE INFRARED PHOTOTHERMAL IMAGING SYSTEM

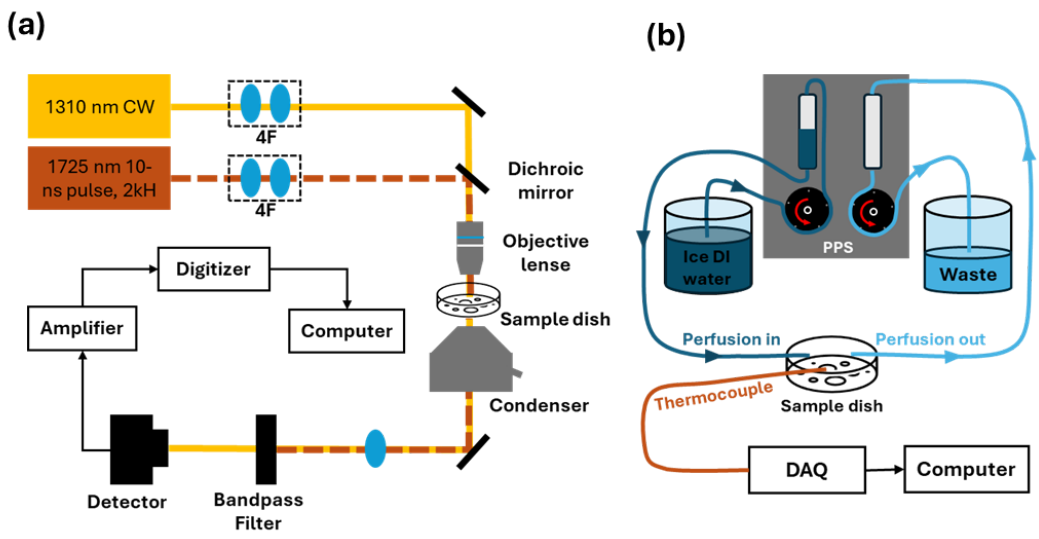


Figure 2. Schematic of a low-temperature shortwave infrared photothermal (SWIP) imaging system. (a) Schematic of the SWIP microscope used for photothermal imaging. (b) An independent temperature regulation setup used to cool the sample during low-temperature experiment. PPS: peristaltic perfusion system.

Our setup integrates the SWIP microscope (**Figure 2a**) and a low-temperature regulation system (**Figure 2b**), which operate simultaneously. The SWIP microscope enables chemical imaging, while the temperature regulation system maintains a stable low temperature within the sample dish. The SWIP microscope operates with a pump-probe configuration (**Figure 2a**). A 1725-nm pulsed laser is used as the excitation source to target the first overtone absorption of carbon-hydrogen (C-H) vibrational modes, while a 1310-nm continuous-wave laser serves as the probe beam. The excitation and probe beams are spatially overlapped and focused into the sample, where absorption by specific molecular bonds induces localized heating and results in a thermo-optic effect, which alter the RI and forms a transient microlens that perturbs the propagation of the probe beam. This modulation of the probe is detected through a small aperture

placed at the back focal plane of the condenser, enabling sensitive detection of the photothermal signal.

A peristaltic perfusion system (PPS2, MultiChannel Systems) was used to lower the sample temperature by continuously circulating an ice water/solution through the imaging chamber (**Figure 2b**). While the system does not provide active temperature control, it enables passive cooling of the sample without disturbing the optical setup. A T-type thermocouple thermal sensor was positioned near the imaging area to monitor the temperature in real time. Imaging was performed once the temperature reached a stable level. The temperature reachable with perfusion ranged from 10-14°C, which was the practical lower limit of the current cooling system. The exact temperature that can be reached depends on the ambient temperature in a specific day. To reach higher than ambient temperature, we replaced warm solution to ice solution in the perfusion system.

4 RESULTS

4.1 Performance of Low-Temperature SWIP Spectroscopy and Microscopy

With the temperature controlled SWIP system built, we first characterized the temperature-dependent behavior of PT signals from DI water. Raw time-dependent SWIP traces of water acquired at different temperatures reveal a decrease in SWIP intensity with decreasing temperature (**Figure 3a**). We then computed the mean SWIP intensity across 2500 traces (**Figure 3b**) and observed a linear temperature dependence ($R^2 > 0.95$), which is consistent with our theoretical framework presented in Equation 7.

To evaluate the extent of water background reduction in imaging, we examined 2 μm polystyrene beads suspended in DI water under two temperature conditions: ambient temperature

(20.1°C) and low temperature (12.6°C) (**Figure 3c** and **3d**, respectively). Lateral profiles of a single bead (**Figure 3e**) revealed a decrease in both SWIP signal and background at low temperature. To further quantify this effect, we plotted the mean SWIP traces from polystyrene and water-rich regions of interest (ROIs) at ambient temperature (**Figure 3f**) and low temperature (**Figure 3g**). Although both signal and background decrease with cooling, imaging at low temperature improves S/B by 2.3 fold compared to ambient temperature.

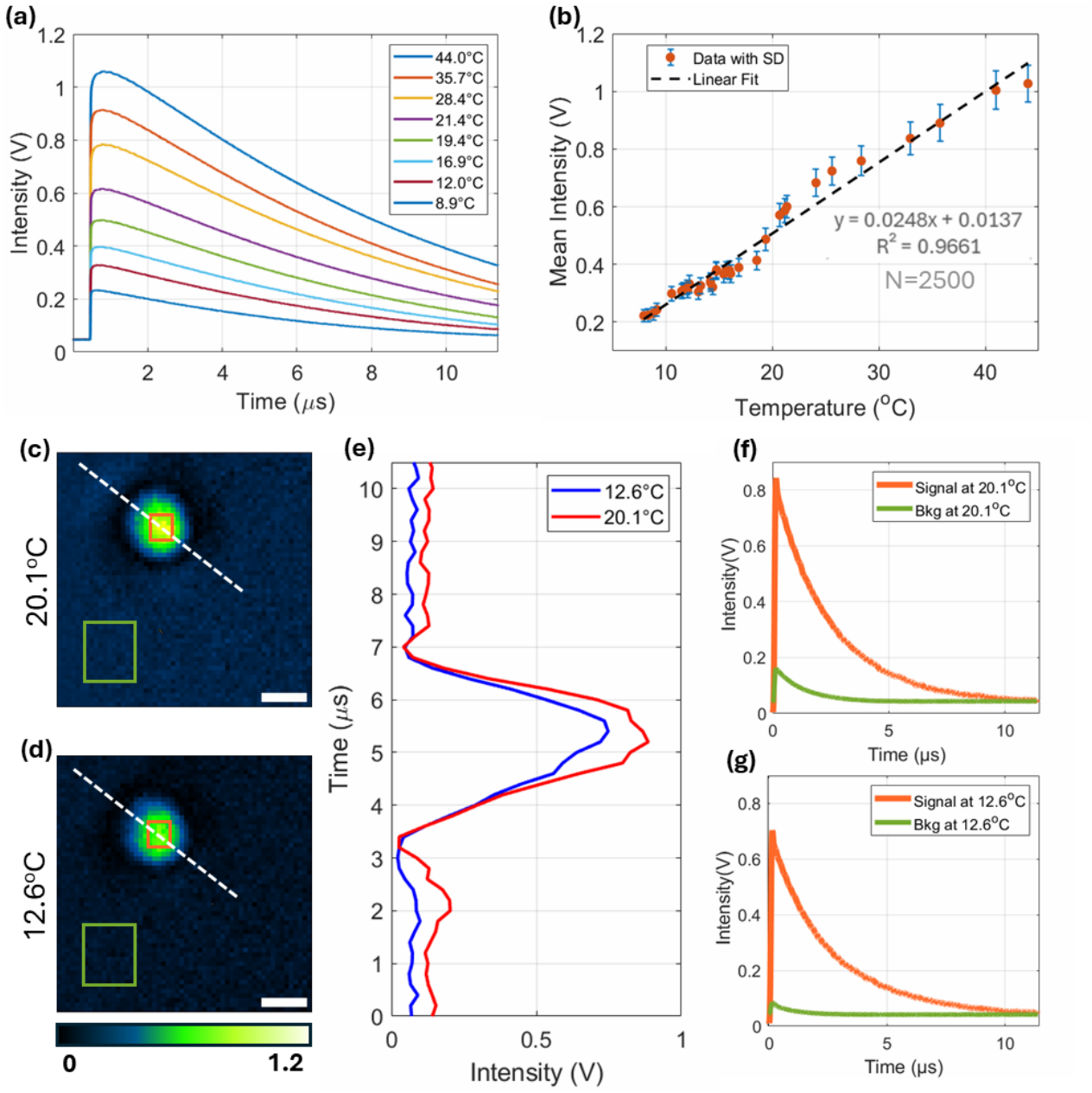


Figure 3. Low-temperature SWIP suppresses the background signal. (a) SWIP trace of DI water measured at different temperatures. (b) Linear fit of mean SWIP intensity from DI water (N = 2500) as a function of temperature. (c), (d) SWIP images of 2 µm polystyrene beads in DI water acquired at 20.1°C and 12.6°C, respectively. Scale bar 2 µm. (e) Intensity profiles along the dashed lines in panels (c) and (d). (f), (g) Mean SWIP traces of ROI of bead shown in (c) and (d), corresponding to their respective temperatures.

4.2 Temperature-controlled SWIP Imaging of U87 Cells

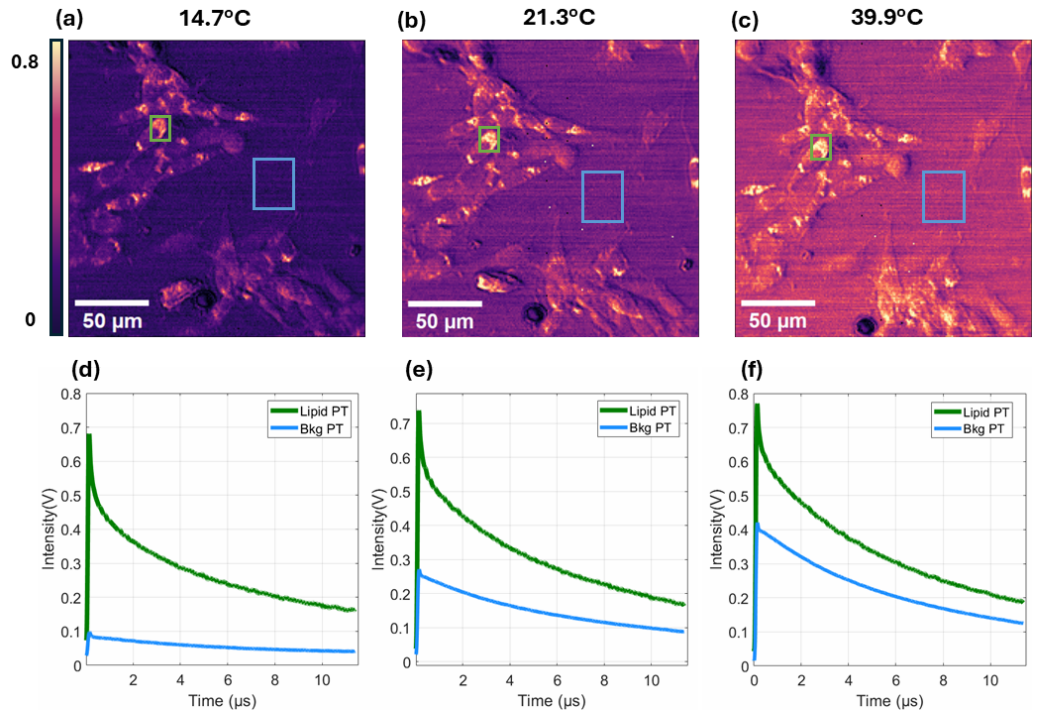


Figure 4: Temperature-controlled SWIP imaging of U-87 MG cells treated with 100 µM OA. (a)-(c), SWIP images of U-87 cells acquired at 14.7°C, 21.3°C, 39.9°C, respectively. Scale bar 50µm. (d)-(f), SWIP traces from lipid-rich regions and background areas corresponding to the temperatures in (a)-(c).

With the method established, we then evaluated the contrast dependence on temperature in a cellular imaging experiment. We imaged U-87 MG cells under varying temperature conditions after treatment with 100 μM oleic acid for 24 hours to increase lipid droplet content. During imaging, we observed a shift in the focal plane across different temperatures attributed to the temperature dependence of the refractive index (RI), which alters the optical path length (OPL). To ensure accurate comparison across conditions, the focal plane was manually adjusted for each temperature setting (Figure S1). As demonstrated in Figure 4a-c, progressive cooling from 39.9°C to 21.3°C and finally to 14.7°C resulted in dramatic background suppression while preserving lipid-rich cellular features. Signal-to-background (S/B) ratios show that reducing sample temperature from 39.9°C to 21.3°C improves the ratio by 1.6-fold, with further cooling to 14.7°C achieving a 5.5-fold enhancement. Time-domain SWIP traces (Figure 4d-f) revealed the underlying mechanism: while the background photothermal signal from water decreased by 1.5-fold and 4-fold at 21.3°C and 14.7°C, respectively (relative to 39.9 °C), the lipid-associated photothermal signal remained remarkably stable across all temperatures. This temperature-dependent background suppression enables enhanced visualization of lipid distributions in vivo cell culture.

4.3 Low Temperature versus Ambient Temperature SWIP Imaging of 3D Specimens

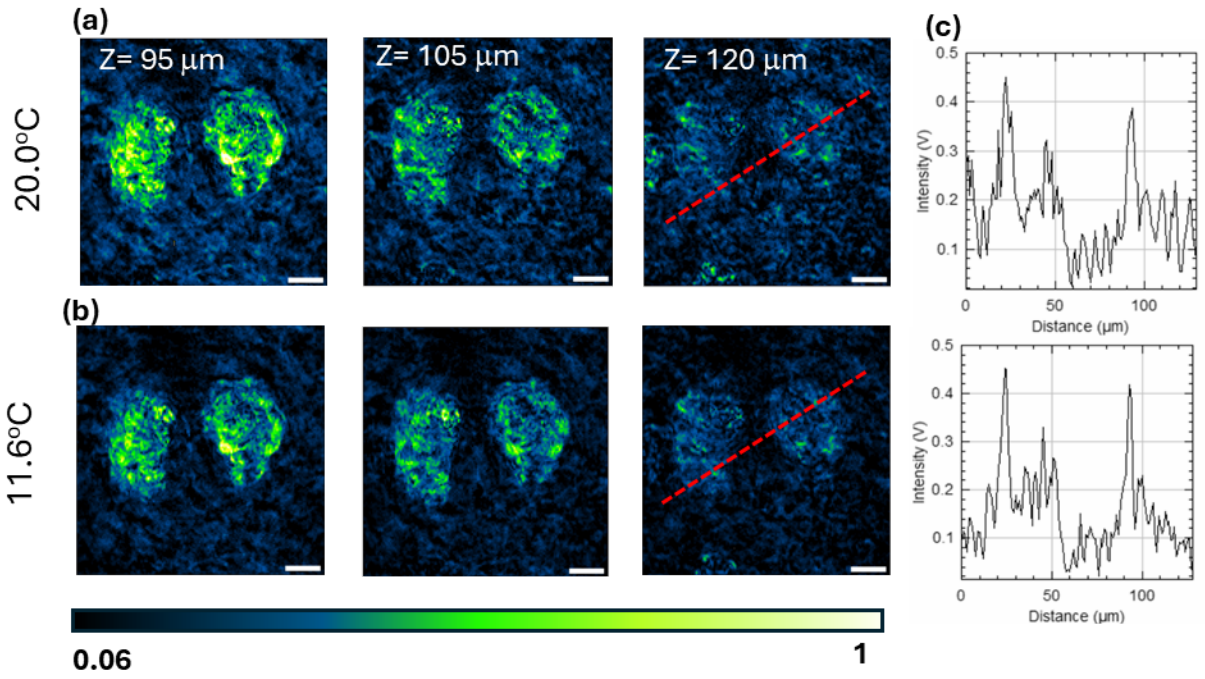


Figure 5. SWIP imaging of a mouse ear tissue at two temperature conditions. (a) SWIP image of a sebaceous gland in the mouse ear acquired at ambient temperature (20.0°C). (b) SWIP image of the same region acquired at low temperature (11.6°C). Scale bar 20µm. (c) Intensity profiles along the dashed line in a and b, extracted at imaging depth Z=120 µm.

To assess the impact of temperature on deep tissue imaging contrast, we acquired SWIP images of a mouse ear tissue at various depths, focusing on a sebaceous gland (**Figure 5**). At ambient temperature (**Figure 5a**), strong background signals obscure the gland boundary, especially at greater depths, where the weak lipid signal becomes comparable to the background. In contrast, low-temperature imaging (**Figure 5b**) enhances the visibility of these structures by effectively suppressing background, resulting in clearer gland boundaries. The contrast-to-noise ratio (CNR), defined as the difference between the mean signal intensity and the mean background intensity divided by the standard deviation of the background, increases for a low-

lipid ROI showed an increase from 0.4 to 2.0 at Z = 95 µm, from 0.9 to 1.9 at Z = 105 µm, and from 0.5 to 1.8 at Z = 120 µm under cooling. These results demonstrate that lowering temperature significantly enhances the contrast of weak lipid signals deep in tissue. Lateral intensity profiles (**Figure 5c**, top panels) further illustrate improved separation between the gland and the background under low-temperature conditions.

4.4 Low-temperature MIP Imaging Suppresses Background in the Fingerprint Window

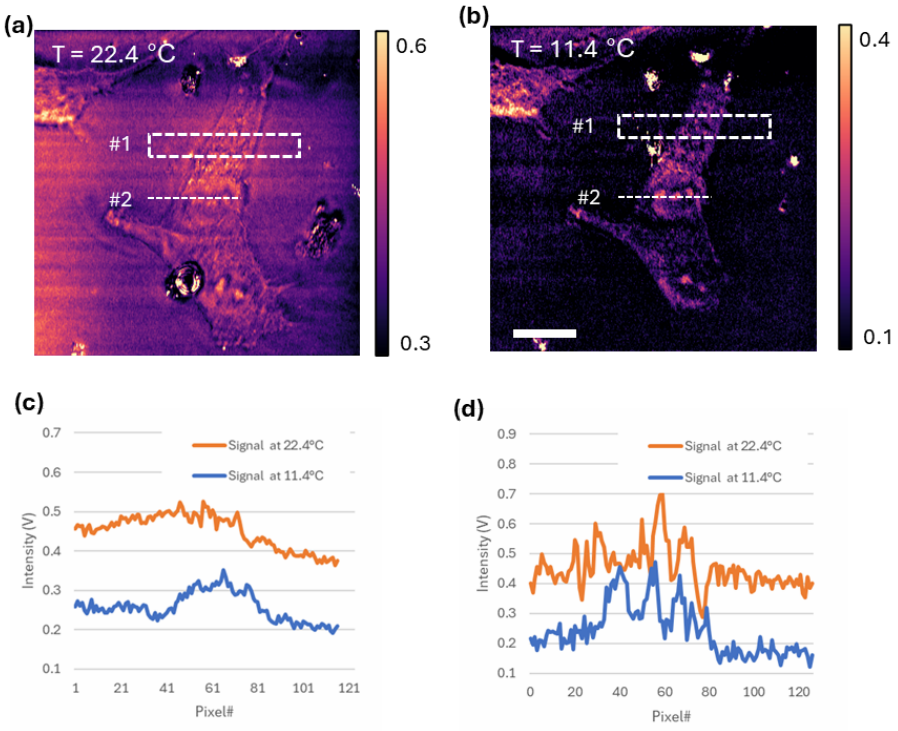


Figure 6. Low-temperature mid-infrared photothermal (MIP) imaging of U87 MG cells. (a), (b) MIP images of cells acquired at 22.4°C, 11.4°C, respectively while exciting the amid-I band (1650 cm^{-1}). (c) Average signal extracted from ROI #1 in the cytoplasm at two temperature conditions. (d) Intensity profile along ROI #2 across cell nucleus at two temperature conditions. Scale bar: 20µm

To demonstrate that low-temperature background suppression is a generalizable strategy across photothermal imaging platforms, we extend our approach to mid-infrared photothermal (MIP) microscopy where water background is severe for samples in aqueous environment. The mid-infrared (MIR) region contains richer molecular information than shortwave infrared regime, for example, by excite the amide-I band, MIR spectrum can detect the subtle protein secondary structure. However, due to the strong and overlapping absorption of water at 1650 cm^{-1}, high contrast MIP imaging of proteins is typically achieved only by substituting H_2O based PBS with D_2O one, making it hardly be applied in living cells. Here, by implementing the low temperature strategy, we have improved the SBR by 2.8-fold in amide-I band imaging of cells in phosphate buffer solution (PBS).

For performing this low temperature MIP imaging, we integrated the same temperature regulation setup above with a counter-propagating MIP microscope. In this experiment, we imaged U-87 MG cells in PBS under two temperature conditions which are ambient temperature (22.4°C) and low temperature (11.4°C), while targeting the amide-I vibrational band at 1650 cm^{-1}. The focal plane was manually adjusted between two temperature conditions.

At ambient temperature, cellular protein contents show minimal contrast (**Figure 6a**) as the MIP signal is dominated by water background arising from overlap between amide-I absorption and the O-H bending mode of water. By cooling to 11.4°C, the cell contrast is markedly enhanced (**Figure 6b**), with water the background reduced approximately by half. As a result, subcellular features become clearly visible, including the nucleus, which is known as protein aggregation. The MIP signal profile analysis across the cytoplasm and nucleus reveals that 2.6-fold and 2.8-fold improvements in S/B respectively when lowering the temperature from 22.4°C

to 11.4°C (**Figure 6c, d**). Together, these data show effective background suppression in MIP microscopy by lowering the imaging temperature.

5 CONCLUSION AND DISCUSSION

Our findings demonstrate that low-temperature measurement in SWIP microscopy effectively reduces background interference, thereby enhancing the contrast and visibility of weak photothermal signals, particularly at deeper layers in 3D biological samples. By lowering the sample temperature using a perfusion system, we achieved substantial improvements in signal-to-background ratio (S/B) and contrast-to-noise ratio (CNR) across multiple model systems, confirming the broad applicability of this approach for high-contrast, label-free imaging in depth-resolved applications.

This advantage is particular important because, in previous reported 3D SWIP imaging [14], the raw signal at each pixel is assumed to contain both the desired SWIP signal and background contributions. To improve the S/B in thick biological samples, pixel-wise post processing is therefore required. In particular, the temporal trace at each pixel is fitted with a biexponential model, and the component with the slower photothermal decay is subtracted as background, as described in [14]. Although this approach can improve SBR, it is computationally intensive, and the decay threshold used to distinguish SWIP signal from background is image dependent rather than universal. In contrast, the low-temperature approach selectively suppresses the water-induced background at the source, thereby enhancing SBR without the need for post-acquisition data processing

Beyond SWIP, the verified temperature dependency of water photothermal signal provides foundations for developing further background reduction techniques in other types of photothermal microscope. This concept is particular valuable in mid-infrared photothermal

microscope, where the water absorption is a significant source of background, especially in the amide I band region and in the spectrally silent window[21].

We also found that it does not improve the limit of detection in photothermal spectroscopy of liquid specimens (Supplementary S4, Figure S2). In homogeneous liquid systems such as D O/DMSO mixtures, cooling reduces the photothermal responses of both solvent and solute simultaneously, resulting in a uniform decrease in overall SWIP signal rather than selective background suppression. This observation highlights that the benefit of low-temperature operation primarily arises in heterogeneous samples, such as cells or tissues, where differential thermal responses between water and biomolecular components can be exploited to enhance contrast

While our temperature-control approach enhances the photothermal contrast, there is space to improve. First, as noted above, 10-14°C represents the practical lower limit of the current cooling system. However, based on the temperature dependence of water's refractive index reported by Tilton and Taylor[29], the change in water RI become very small below 4°C. Therefore, we expect that achieving stable sample temperatures closer to 4°C could further suppress the water background and improve the image contrast. Secondly, the current setup lacks precise temperature control; integrating active temperature regulation would enable more stable and tunable temperature-imaging conditions. A more precise and stable controlled temperature imaging experiment can be designed by employing thermoelectric cooler with feedback. Additionally, development of a temperature-stabilized SWIP system will allow broader applications, including high-resolution chemical mapping in intact 3D tissues, and quantitative studies of temperature-sensitive biomolecular dynamics. Future works could explore SWIP

imaging of proteins via the N-H vibration band which strongly overlaps with water absorption and would benefit from this background suppression approach.

We note lowering the temperature for a long period would alter cell metabolism. This method is suitable for fixed cells, fresh frozen tissues, or immediate measurements of live cells. Meanwhile, in model organisms such as *C. elegans* and zebrafish embryos, mild cooling reduces motion artifacts and photothermal damage, extending imaging durations without compromising viability. With attempting to apply the low temperature strategy the 3D model like *C. elegans*, low-temperature SWIP significantly suppresses background and enhances contrast at increasing depths, enabling the visualization of weak lipid droplets that are otherwise obscured at ambient temperature, particularly in deeper layers (Supplementary S5, Figure S3).

ASSOCIATED CONTENT

Supporting Information

The Supporting Information file is submitted, details the SWIP and MIP microscope configurations, temperature-controlled imaging using a TEC feedback system, and cell/tissue preparation methods. It presents a theoretical framework linking photothermal signal to temperature-dependent refractive index changes. Additional experiments show temperature-induced focal shifts, evaluate detection limits in DMSO/D O solutions, and demonstrate improved contrast and deeper imaging in *C. elegans* at low temperatures due to effective background suppression.

Code, Data, and Materials Availability

All data in the main text and the supplementary are available via GitHub (https://github.com/pnnthao-cloud/Background-suppressed-Infrared-Photothermal-Microscopy-at-Low-Temperature)

AUTHOR INFORMATION

Corresponding Author

Ji-Xin Cheng - Department of Electrical & Computer Engineering, Boston University, Boston, MA, 02115, US; Photonics Center, St. Mary, Boston, MA, 02115, US

Authors

Thao N. Pham - Department of Biomedical Engineering, Boston University, Boston, MA, 02115, US

Jiaze Yin - Department of Electrical & Computer Engineering, Boston University, Boston, MA, 02115, US

Yuhao Yuan - Department of Electrical & Computer Engineering, Boston University, Boston, MA, 02115, US; Photonics Center, St. Mary, Boston, MA, 02115, US

Dingcheng Sun - Department of Biomedical Engineering, Boston University, Boston, MA, 02115, US

Bethany Weinberg - Graduate Program of Molecular Biology, Cell Biology, and Biochemistry, Boston University, Boston, MA, 02215, US

Hongli Ni - Department of Electrical & Computer Engineering, Boston University, Boston, MA, 02115, US

Author Contributions

* T.N.P and J.Y. contributed equally to this work. T.N.P. conducted experiments, processed the SWIP data, helped with building PT temperature dependency theorical equation, performed experiments, and drafted the paper. J.Y. conducted the PT temperature dependency theorical equation built the temperature regulation system, collected and processed MIP data and was involved in manuscript writing and editing. Y.Y. and H.N. built the SWIP microscope. D.S. performed cell culture, treatment and sample preparation, and was involved in manuscript writing and editing. B.W. performed all worm culture and sample preparation, as well as assisting with manuscript writing and editing. J.X.C. initiated the project, revised the manuscript, and provided scientific guidance. All authors revised the manuscript.

Notes:

JXC declares financial interest with Photothermal Spectroscopy Corp which did not fund this work. Other authors declare that there are no financial interests, commercial affiliations, or other potential conflicts of interest that could have influenced the objectivity of this research.

ACKNOWLEDGMENTS

This work is supported by R35GM136223 to JXC.

REFERENCES

(1) Ben-Dor, E.; Inbar, Y.; Chen, Y. The Reflectance Spectra of Organic Matter in the Visible Near-Infrared and Short Wave Infrared Region (400–2500 Nm) during a Controlled Decomposition Process. *Remote Sensing of Environment* **1997**, *61* (1), 1–15. https://doi.org/10.1016/S0034-4257(96)00120-4.

(2) Hansen, M. P.; Malchow, D. S. Overview of SWIR Detectors, Cameras, and Applications. In *Thermosense XXX*; SPIE, 2008; Vol. 6939, pp 94–104. https://doi.org/10.1117/12.777776.

(3) Tsuboi, S.; Jin, T. Shortwave-Infrared (SWIR) Fluorescence Molecular Imaging Using Indocyanine Green–Antibody Conjugates for the Optical Diagnostics of Cancerous

Tumours. *RSC Advances* **2020**, *10* (47), 28171–28179. https://doi.org/10.1039/D0RA04710D.

(4) Feng, J.; Rogge, D.; Rivard, B. Comparison of Lithological Mapping Results from Airborne Hyperspectral VNIR-SWIR, LWIR and Combined Data. *International Journal of Applied Earth Observation and Geoinformation* **2018**, *64*, 340–353. https://doi.org/10.1016/j.jag.2017.03.003.

(5) O'Sullivan, T. D.; Leproux, A.; Chen, J.-H.; Bahri, S.; Matlock, A.; Roblyer, D.; McLaren, C. E.; Chen, W.-P.; Cerussi, A. E.; Su, M.-Y.; Tromberg, B. J. Optical Imaging Correlates with Magnetic Resonance Imaging Breast Density and Reveals Composition Changes during Neoadjuvant Chemotherapy. *Breast Cancer Res* **2013**, *15* (1), R14. https://doi.org/10.1186/bcr3389.

(6) Torjesen, A.; Istfan, R.; Roblyer, D. Ultrafast Wavelength Multiplexed Broad Bandwidth Digital Diffuse Optical Spectroscopy for in Vivo Extraction of Tissue Optical Properties. *Journal of Biomedical Optics* **2017**, *22* (3), 036009. https://doi.org/10.1117/1.JBO.22.3.036009.

(7) Zhao, Y.; Pilvar, A.; Tank, A.; Peterson, H.; Jiang, J.; Aster, J. C.; Dumas, J. P.; Pierce, M. C.; Roblyer, D. Shortwave-Infrared Meso-Patterned Imaging Enables Label-Free Mapping of Tissue Water and Lipid Content. *Nat Commun* **2020**, *11* (1), 5355. https://doi.org/10.1038/s41467-020-19128-7.

(8) Horton, N. G.; Wang, K.; Kobat, D.; Clark, C. G.; Wise, F. W.; Schaffer, C. B.; Xu, C. In Vivo Three-Photon Microscopy of Subcortical Structures within an Intact Mouse Brain. *Nature Photon* **2013**, *7* (3), 205–209. https://doi.org/10.1038/nphoton.2012.336.

(9) Shi, L.; Zheng, C.; Shen, Y.; Chen, Z.; Silveira, E. S.; Zhang, L.; Wei, M.; Liu, C.; de Sena-Tomas, C.; Targoff, K.; Min, W. Optical Imaging of Metabolic Dynamics in Animals. *Nat Commun* **2018**, *9* (1), 2995. https://doi.org/10.1038/s41467-018-05401-3.

(10) Salinas, C. M.; Reichel, E.; Witte, R. S. Short-Wave Infrared Photoacoustic Spectroscopy for Lipid and Water Detection. In *2021 IEEE International Ultrasonics Symposium (IUS)*; 2021; pp 1–4. https://doi.org/10.1109/IUS52206.2021.9593904.

(11) Li, Z.; Huang, S.; He, Y.; Wijnbergen, J. W. van; Zhang, Y.; Cottrell, R. D.; Smith, S. G.; Hammond, P. T.; Chen, D. Z.; Padera, T. P.; Belcher, A. M. A New Label-Free Optical Imaging Method for the Lymphatic System Enhanced by Deep Learning. bioRxiv January 15, 2023, p 2023.01.13.523938. https://doi.org/10.1101/2023.01.13.523938.

(12) Swinehart, D. F. The Beer-Lambert Law. *J. Chem. Educ.* **1962**, *39* (7), 333. https://doi.org/10.1021/ed039p333.

(13) Bigio, I. J.; Fantini, S. *Quantitative Biomedical Optics: Theory, Methods, and Applications*; Cambridge Texts in Biomedical Engineering; Cambridge University Press, 2016. https://doi.org/10.1017/CBO9781139029797.

(14) Ni, H.; Yuan, Y.; Li, M.; Zhu, Y.; Ge, X.; Yin, J.; Dessai, C. P.; Wang, L.; Cheng, J.-X. Millimetre-Deep Micrometre-Resolution Vibrational Imaging by Shortwave Infrared Photothermal Microscopy. *Nat. Photon.* **2024**, *18* (9), 944–951. https://doi.org/10.1038/s41566-024-01463-6.

(15) Cheng, J.-X.; Yuan, Y.; Ni, H.; Ao, J.; Xia, Q.; Bolarinho, R.; Ge, X. Advanced Vibrational Microscopes for Life Science. *Nat Methods* **2025**, *22* (5), 912–927. https://doi.org/10.1038/s41592-025-02655-w.

(16) Yin, J.; Lan, L.; Zhang, Y.; Ni, H.; Tan, Y.; Zhang, M.; Bai, Y.; Cheng, J.-X. Nanosecond-Resolution Photothermal Dynamic Imaging via MHZ Digitization and Match Filtering. *Nat Commun* **2021**, *12* (1), 7097. https://doi.org/10.1038/s41467-021-27362-w.
(17) Bolarinho, R.; Yin, J.; Ni, H.; Xia, Q.; Cheng, J.-X. Background-Free Mid-Infrared Photothermal Microscopy via Single-Shot Measurement of Thermal Decay. *Anal. Chem.* **2025**, *97* (8), 4299–4307. https://doi.org/10.1021/acs.analchem.4c03689.
(18) Kell, G. S. Precise Representation of Volume Properties of Water at One Atmosphere. *J. Chem. Eng. Data* **1967**, *12* (1), 66–69. https://doi.org/10.1021/je60032a018.
(19) Prakash, J.; Seyedebrahimi, M. M.; Ghazaryan, A.; Malekzadeh-Najafabadi, J.; Gujrati, V.; Ntziachristos, V. Short-Wavelength Optoacoustic Spectroscopy Based on Water Muting. *Proceedings of the National Academy of Sciences* **2020**, *117* (8), 4007–4014. https://doi.org/10.1073/pnas.1910597117.
(20) Xu, C.; Rassel, S.; Zhang, S.; Aloraynan, A.; Ban, D. Single-Wavelength Water Muted Photoacoustic System for Detecting Physiological Concentrations of Endogenous Molecules. *Biomed. Opt. Express, BOE* **2021**, *12* (1), 666–675. https://doi.org/10.1364/BOE.413086.
(21) Zhang, D.; Li, C.; Zhang, C.; Slipchenko, M. N.; Eakins, G.; Cheng, J.-X. Depth-Resolved Mid-Infrared Photothermal Imaging of Living Cells and Organisms with Submicrometer Spatial Resolution. *Science Advances* **2016**, *2* (9), e1600521. https://doi.org/10.1126/sciadv.1600521.
(22) Chapter 3 - Thermo-Optic Coefficients. In *Handbook of Optical Constants of Solids*; Palik, E. D., Ed.; Academic Press: Burlington, 1997; pp 115–261. https://doi.org/10.1016/B978-012544415-6.50150-3.
(23) Kragh, H. The Lorenz-Lorentz Formula: Origin and Early History. *Substantia* **2018**, *2* (2), 7–18. https://doi.org/10.13128/Substantia-56.
(24) Weiss, L.; Tazibt, A.; Tidu, A.; Aillerie, M. Water Density and Polarizability Deduced from the Refractive Index Determined by Interferometric Measurements up to 250 MPa. *J Chem Phys* **2012**, *136* (12), 124201. https://doi.org/10.1063/1.3698481.
(25) Domingo, M.; Luna, R.; Satorre, M. Á.; Santonja, C.; Millán, C. Lorentz–Lorenz Coefficient of Ice Molecules of Astrophysical Interest: N2, CO2, NH3, CH4, CH3OH, C2H4, and C2H6. *Astrophysical Journal* **2021**, *906* (2), 81. https://doi.org/10.3847/1538-4357/abc5c5.
(26) Taylor, M. S.; Becker, M. P. Quantiles of Multi-Sample Smirnov Type Statistics. *Journal of Statistical Computation and Simulation* **1982**, *16* (1), 25–34. https://doi.org/10.1080/00949658208810604.
(27) Thormählen, I.; Straub, J.; Grigull, U. Refractive Index of Water and Its Dependence on Wavelength, Temperature, and Density. *J. Phys. Chem. Ref. Data* **1985**, *14* (4), 933–945. https://doi.org/10.1063/1.555743.
(28) Guillory, J. K. The Merck Index: An Encyclopedia of Chemicals, Drugs, and Biologicals Edited by Maryadele J. O'Neil, Patricia E. Heckelman, Cherie B. Koch, and Kristin J. Roman. Merck, John Wiley & Sons, Inc., Hoboken, NJ. 2006. Xiv + 2564 Pp. 18 × 26 Cm. ISBN-13 978-0-911910-001. $125.00. *J. Med. Chem.* **2007**, *50* (3), 590–590. https://doi.org/10.1021/jm068049o.
(29) Tilton, L. W.; Taylor, J. K. Refractive Index and Dispersion of Distilled Water for Visible Radiation, at Temperatures 0 to 60 Degrees C. *J. RES. NATL. BUR. STAN.* **1938**, *20* (4), 419. https://doi.org/10.6028/jres.020.024.